

Stem Cell Reports, Volume 2

Supplemental Information

A Rapid and Efficient 2D/3D Nuclear Segmentation Method

for Analysis of Early Mouse Embryo and Stem Cell Image Data

Xinghua Lou, Minjung Kang, Panagiotis Xenopoulos, Silvia Muñoz-Descalzo, and Anna-Katerina Hadjantonakis

Inventory

Supplemental Figure

Figure S1. MINS application in the detection of cell division and apoptosis.

2D and 3D fluorescent images and MINS segmentation showing cell division and apoptosis.

Supplemental Tables

Table S1. MINS segmentation accuracy on 2D data.

Results from the analysis of 10 sample 2D data sets through MINS

Table S2. MINS segmentation accuracy on 3D data.

Results from the analysis of 18 sample 3D data sets through MINS.

Supplemental Movies

Movie S1. Segmentation result on the DCellIQ image sequence.

Side-by-side view of segmentation result on the DCellIQ image sequence (3D). Quantitative results are provided in Table 1.

Movie S2. Segmentation result on the Mitocheck image sequence.

Side-by-side view of segmentation result on the Mitocheck image sequence (2D). Quantitative results are provided in Table 1.

Movie S3. Segmentation result on a 3D MK dataset.

Side-by-side view of segmentation result on the MK volume (MK-1). Quantitative results are provided in Table 2.

Movie S4. Segmentation result on a 3D NS dataset.

Side-by-side view of segmentation result on the NS volume (NS-4). Quantitative results are provided in Table 2. This result shows the robustness of MINS against strong background.

Movie S5. Segmentation result on a 3D NS dataset.

Side-to-side view of segmentation result on the NS volume (NS-5). Quantitative results are provided in Table 2. This result shows the robustness of MINS against strong background.

SUPPLEMENTAL DATA

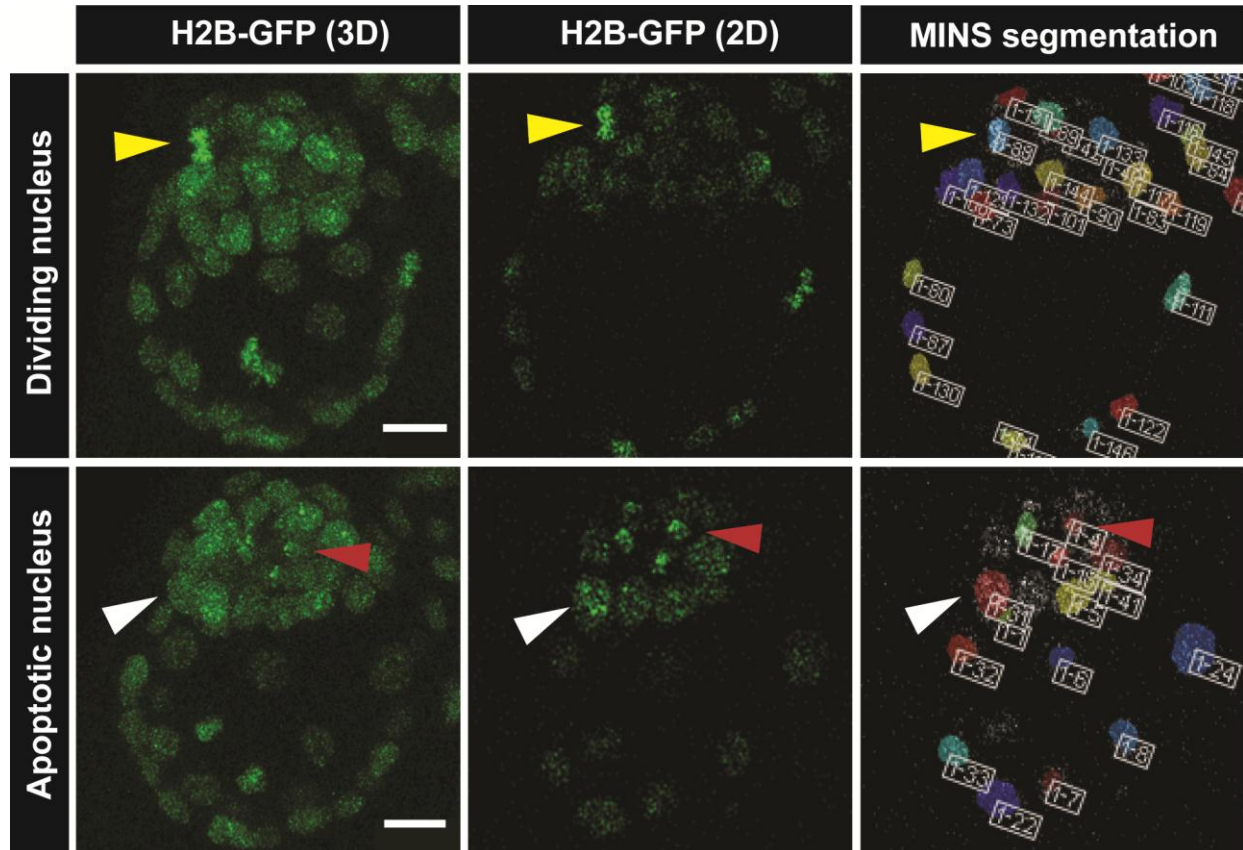


Figure S1. MINS application in the detection of cell division and apoptosis.

2D laser scanning confocal images acquired as z-stacks and 3D renderings from *CAG:H2B-GFP* reporter-expressing embryos, followed MINS segmentation of these data. Yellow arrowhead depicts condensed chromosomes (and increased fluorescence intensity) representing a cell in mitosis detected by MINS (ID #88). Red arrowhead depicts the nuclear debris associated with an apoptotic nucleus. These features have a significantly lower volume than a normal interphase nucleus (ID #4). White arrowhead depicts a nucleus of expected interphase (elipsoid) shape for this stage of embryo (ID #31). Scale bar: 20 μ m.

Table S1. MINS segmentation accuracy on 2D data.

Data	Size	N_{True}	N_{Seg}	N_{TP}	N_{FP}	N_{FN}	Precision	Recall	F-score
DCellIQ (No. 1)	512 x 672	59	59	59	0	0	100.0	100.0	100.0
DCellIQ (No. 2)	512 x 672	72	71	70	1	2	98.6	97.2	97.9
DCellIQ (No. 3)	512 x 672	95	94	93	1	2	98.9	97.9	98.4
DCellIQ (No. 4)	512 x 672	113	114	112	2	1	98.2	99.1	98.7
DCellIQ (No. 5)	512 x 672	145	148	143	5	2	96.6	98.6	97.6
Mitochek (No. 1)	1024 x 1344	119	121	117	4	2	96.7	98.3	97.5
Mitochek (No. 2)	1024 x 1344	157	161	155	6	2	96.3	98.7	97.5
Mitochek (No. 3)	1024 x 1344	241	239	237	2	4	99.2	98.3	98.8
Mitochek (No. 4)	1024 x 1344	306	308	304	4	2	98.7	99.3	99.0
Mitochek (No. 5)	1024 x 1344	460	460	455	5	5	98.9	98.9	98.9

Table S2. MINS segmentation accuracy on 3D data.

Data	Size	N_{True}	N_{Seg}	N_{TP}	N_{FP}	N_{FN}	Precision	Recall	F-score
NS (No. 1)	512 x 512 x 54	63	60	59	1	4	98.3	93.7	95.9
NS (No. 2)	512 x 512 x 59	83	78	78	0	5	100.0	94.0	96.9
NS (No. 3)	512 x 512 x 72	86	81	79	2	7	97.5	91.9	94.6
NS (No. 4)	512 x 512 x 63	81	79	79	0	2	100.0	97.5	98.8
NS (No. 5)	512 x 512 x 60	98	98	96	2	2	98.0	98.0	98.0
PX (No. 1)	512 x 512 x 89	83	83	81	2	2	97.6	97.6	97.6
PX (No. 2)	512 x 512 x 111	84	81	79	2	5	97.5	94.0	95.8
PX (No. 3)	512 x 512 x 106	86	84	83	1	3	98.8	96.5	97.6
PX (No. 4)	512 x 512 x 74	80	76	74	2	6	97.4	92.5	94.9
PX (No. 5)	512 x 512 x 85	67	67	67	0	0	100.0	100.0	100.0
MK (No. 1)	512 x 512 x 28	123	123	122	1	1	99.2	99.2	99.2
MK (No. 2)	512 x 512 x 28	129	130	127	3	2	97.7	98.4	98.1
MK (No. 3)	512 x 512 x 28	128	130	128	2	0	98.5	100.0	99.2
MK (No. 4)	512 x 512 x 28	127	125	124	1	3	99.2	97.6	98.4
MK (No. 5)	512 x 512 x 28	132	129	129	0	3	100.0	97.7	98.9
MK (No. 6)	512 x 512 x 28	122	120	120	0	2	100.0	98.4	99.2
MK (No. 7)	512 x 512 x 28	116	114	112	2	4	98.2	96.6	97.4
MK (No. 8)	512 x 512 x 28	121	121	118	3	3	97.5	97.5	97.5

SUPPLEMENTAL EXPERIMENTAL PROCEDURES

Cell cultures and live imaging.

XEN cell media is high glucose Dulbecco's modified Eagle's media (D-MEM, Gibco) supplemented with 20% fetal bovine serum (FBS), 0.1 mM 2-mercaptoethanol, 1 mM non-essential amino acids, 1 mM sodium pyruvate, 2 mM glutamine, 100 units/mL penicillin and 100 µg/mL streptomycin. ES cell media are the same as XEN cell media but supplemented with recombinant leukemia inhibitory factor (LIF) (Mereau et al., 1993). XEN cells were cultured on gelatin-coated plates and ES Cells were cultured in the presence of mouse embryonic fibroblast (MEF) feeders at 37°C in 5% CO₂. For live imaging, cells were plated on a gelatin-coated glass bottom dishes (MatTek) and maintained in an environmental chamber (Solent Scientific), as previously described (Kang et al., 2013).

Embryo collection, *in vitro* embryo culture and staining.

Mice were maintained under a 12-hour light/dark cycle. Embryos were recovered in M2 media (Millipore). For live imaging, embryos were cultured in KSOM media (Millipore) under mineral oil (Sigma) on agarose-coated glass-bottom dishes (MatTek) in an environmental chamber (Solent Scientific) maintaining 37°C and 5% CO₂, 5% O₂ and 90% N₂. Embryos were fixed in 4% paraformaldehyde (PFA) in PBS for 10 minutes at room temperature or overnight at 4°C, permeabilised in 0.5% Triton X-100 in PBS for 20 minutes and blocked in 2% horse serum in PBS for 1 hour at 4°C. Immunostaining was performed using various protocols as previously described (Artus et al., 2010; Nichols et al., 2009; Plusa et al., 2008). DNA was stained and visualized using Hoechst 33342 (5 µg/ml, Invitrogen).

Image data acquisition.

Laser scanning confocal images were acquired as z-stacks of optical sections on a Zeiss LSM510META (static 3D, time-lapse 3D) or LSM700 (time-lapse 3D). Fluorescence was excited with a 405-nm laser diode (Hoechst), a 488-nm Argon laser (GFP), a 543-nm HeNe laser (Alexa-Fluor-543/555) and a 633-nm HeNe laser (Alexa-Fluor-633/647). Images were acquired using a Plan-apochromat 20x/NA 0.75, Plan-Neofluar 40x/1.30 or Plan-apochromat 63x/1.40 with optical section thickness of 0.5-2 µm. For 3D rendering, raw data were processed using Zeiss AIM/ZEN software (Carl Zeiss Microsystems) or IMARIS 7.2.2 software (Bitplane AG).

Algorithmic components of MINS.

1. Detection

The detection of nuclei, based on the assumption that cells are generally bright, blob-like objects, resembles a well-studied computer vision problem - blob detection (Forsyth and Ponce, 2002). The performance of the detection procedure is determined by the degree of overlap between proximate nuclei, the variability of size, and the irregularity of shape and texture.

For the detection of nuclei within samples we apply the Hessian eigenvalue thresholding method introduced previously (Lou et al., 2012). As shown in **Figure 2**, we first convolve the image with a Gaussian kernel to smooth out noise and weaken local texture. We then compute the Hessian representation and threshold its eigenvalues to extract the foreground, followed by a connected component analysis to extract each nucleus. Finally, this procedure is repeated with a wider Gaussian kernel, and only pixels that are consistently segmented as foreground across all scales are preserved.

Intuitively, Gaussian smoothing aggregates mass from the neighborhood and “pushes” up the central regions of the blobs, which become local maxima. Hessian representation is then used to identify the local maxima because a local maximum has all negative Hessian eigenvalues, while a stationary point (e.g. a saddle point) does not (Gonzales and Woods, 2008). Therefore, simple thresholding of the eigenvalues can extract the foreground (nuclei). This procedure is repeated at different scales, because a large Gaussian kernel strongly suppresses noise, but yields merge error (i.e. under-segmentation, because mass is aggregated from a larger range), while a small Gaussian kernel is sensitive to noise, but better preserves the boundary. Specifically, small smoothing kernel reveal fine structures of the image (i.e. each and every nucleus) well, but are susceptible to noise which eventually leads to false positives (e.g. those in the middle of **Figure 2Ci**). By contrast, a large smoothing kernel can suppress noise, but is suboptimal in separating nuclei (see merged nuclei in **Figure 2Ciii**). The results at different scales are complementary to each other, and combining them produces fewer false positives and merge errors.

In practice, users only need to provide a rough estimate of the average radius of nuclei within the sample imaged, and the MINS program automatically converts this input into parameters. Should the estimate of radius be too small, Gaussian kernel is subject to local texture and prone to split error, resulting in over-segmentation. This can be corrected by increasing the estimation of radius. By contrast, if the radius estimate is too large, proximate

nuclei may be merged, resulting in under-segmentation, and users need to adjust the input parameters by reducing the estimation of radius.

2. Segmentation

The results from detection are then input into the segmentation routine, which is addressed as a seeded multi-label image segmentation problem.

Geodesic Image Segmentation and Fast Marching. A large number of segmentation algorithms are available. For our purposes, and in particular for its runtime consideration, we choose geodesic image segmentation as our base algorithm (Bai and Sapiro, 2007; Couprie et al., 2010; Criminisi et al., 2008). Geodesic image segmentation applies a geodesic distance transform over a grid graph that represents the image. In particular, geodesic distance between two nodes is the shortest path over a grid graph where the edges are weighted according to the continuity of neighboring pixels. Therefore, geodesic image segmentation is also referred to as a shortest path segmentation. Intuitively, given seeds, a new pixel will be assigned with the label of the “closest” seed.

Parallel Geodesic Segmentation. In a multi-label segmentation task, we first assign a unique label to each detected nucleus. A straightforward extension to multi-label segmentation is to transform the problem into a series of binary segmentation tasks: let label i be foreground and the rest background, perform binary geodesic segmentation, and repeat this procedure for each label i . Given an image of m cell nuclei, this gives overall complexity $O(m n \log(n))$, where $O(n \log(n))$ is the complexity of a single geodesic segmentation run using the fast marching method (Hassouna and Farag, 2007; Sethian, 1996), and m is the number of seeds (viz. nuclei). Unfortunately, this one-versus-rest strategy is highly expensive, because in practice m can be large.

To accelerate multi-label geodesic segmentation, we expect to be able to simultaneously propagate multiple labels without causing under-segmentation when those labels are well

scattered and background seeds exist between them. Therefore, we propose the following accelerated multi-label geodesic segmentation:

0. Perform the detection step (**Figure 3B**) on the raw image (**Figure 3A**).

1. Extract the centers of each uniquely labeled nucleus and perform a Delaunay triangulation on the resulting center cloud. This yields an adjacency graph that encodes neighborhood information of all nuclei (**Figure 3C**).

2. Perform graph coloring (Brelaz, 1979) on the adjacency graph, which deterministically assigns different colors to neighboring vertices using as few colors as possible (**Figure 3D**). **3.** Randomly sample pixels below certain intensity threshold as fixed background seeds.

4. Select a color. Let all vertices (viz. labels) having the selected color be foreground and the rest be background in addition to those sampled background seeds, perform a binary geodesic segmentation. Repeat this module for all colors (**Figure 3E**).

5. Re-label the resulting foreground pixels (contain multiple nuclei) by nearest neighbor search with respect to the original detection (**Figure 3F**).

6. Repeat steps 4–5 for each color.

This procedure is illustrated in **Figure 3** on three types of input images. Given raw image and detection results, the first two-step yield clusters of cell nuclei and each cluster contain well scattered nuclei. Binary geodesic segmentation accurately extracts the boundaries of nuclei colored yellow, and the foreground pixels are relabeled with their original label from the detection. After iterating through all colors, the final segmentation is obtained by combining the result from each individual run.

Complexity Analysis. Our accelerated multi-label geodesic segmentation algorithm has a complexity of $O(k n \log(n))$ where k is the number of colors used by the graph coloring. It should be noted that this provides a significant runtime improvement over the naive approach detailed above, because $k \ll m$. More importantly, k does not scale as much as m does (linearly). In detail, the four color theorem states that every planar graph is four-colorable (Appel and Haken, 1989), which means that $k \leq 4$ for 2D segmentation and suggests $O(n \log(n))$ for our multi-label segmentation algorithm in 2D. This property does not transfer to the 3D case – in theory the maximum number of colors needed depends on the surface’s Euler characteristic (Ringel and Youngs, 1968). However, in practice we found that k is usually less than 8 and m is usually between 60 and 100, which normally brings a speed up by a factor of 8 to 10.

3. Classification

Multiple Embryo Separation. To extract multiple embryos present within the same image, we follow a clustering based approach. This problem becomes difficult when false detections emerge from background structures. This prevents us from using methods such as k-means or normalized-cut because of their sensitivity to noise. This stems from the pre-fixed number of clusters required by those methods. Noise will just “pull” clusters towards them, yields untidy clusters or split of true clusters (viz. embryos). In other words, false detections may “drag” the separation hyperplanes towards them and subsequently split true embryos.

Instead, we use mean-shift. The key is noticing that the kernel width of mean-shift naturally corresponds to the embryo size. This allows one to encode embryo shape into mean-shift, which yields a density map where each mode directly corresponds to a clean embryo or a clear pack of false detection. By tracing the modes, mean-shift can identify all embryos and packs of false detections, if any. Given expected number of embryos K , we accept the top K strongest modes as embryo, and the rest should be noise. This is reasonable since usually only embryos exhibit an oval shape that leads to strong mode in the resulting density map.

Note that seeds for mode tracing are randomly chosen in mean-shift. This leads to a mild degree of instability, particularly at the vicinity of two close embryos. For better robustness, we improve mean-shift clustering using the spirit of ensemble learning. Briefly, we run mean-shift multiple times and take the majority vote to decide whether two nuclei belong to the same cluster (viz. embryo).

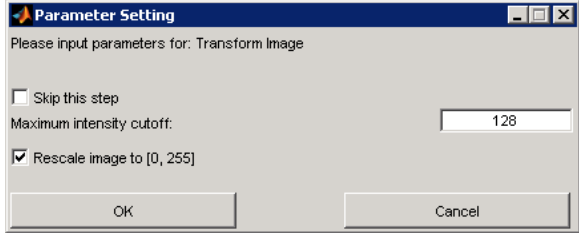
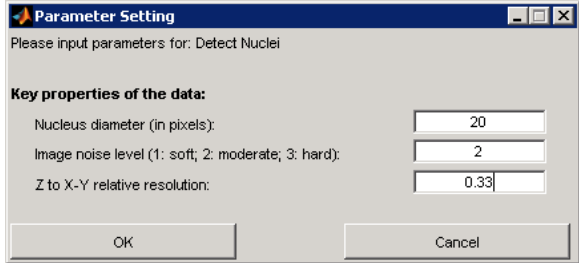
Outlier Removal. Outlier removal is performed per embryo. To do this, we use a robust shape-fitting approach, using ellipse as the underlying shape model. Robust fitting is necessary because false detections that survived the mean-shift embryo extraction will significantly distort the estimation of embryo outline. Our approach consists of two components: RANdom SAmples Consensus (RANSAC) and 2D/3D ellipse fitting.

RANSAC is a robust model estimation framework that can discard outliers by iteratively refining the set of “inlier” detections. Briefly, RANSAC starts by assuming a set of “inliers” using random sampling from all data points. In our case, data points are the coordinates of foreground pixels. It then fits the model (a 2D or 3D ellipsoid) to this set of “inliers” and uses the estimated model parameter to improve the set of “inliers” by filtering out data points in the assumed set of “inliers” that appear incompatible with the estimated model and by adding new ones from the rest that are compatible. This procedure is repeated until convergence. Given a percentage of

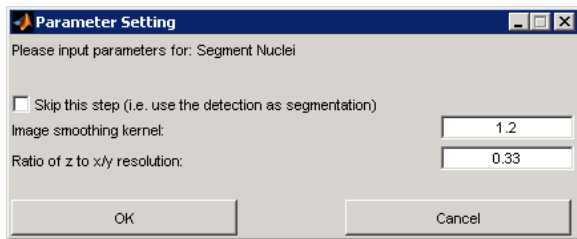
outliers in the data and an expected probability of final success, one can theoretically estimate the upper bound on the number of iterations required. Given a robust model estimation procedure as RANSAC, we are left with finding an algorithm to fit ellipses to 2D/3D data points. We use the method described in (Fitzgibbon et al., 1999), extended to handle 3D data.

ICM versus TE Cell Classification. ICM/TE cell classification relies on the same approach used in the outlier removal step. Essentially, we attempt to fit an ellipse model to the data and this ellipse model describes the border of the embryo. After model estimation, we extract iso-surface at threshold T and consider all cell nuclei that are enclosed by this iso-surface as ICM cells and the rest of the nuclei represent TE cells. It should be noted, that $T = 1$ exactly corresponds to the surface of an ellipse. But in practice we choose $T < 1$ (e.g. 0.98, surface of a shrunk ellipse) for better robustness.

4. MINS Key Parameters by Module

Module	Key Parameters
<p>Module #2: Enhance Image</p> 	<p>1. Maximum Intensity Cutoff: Set this parameter to perform a nonlinear intensity transformation if your image is too dark. In detail, all pixels' intensity is bounded to the given cutoff value and the result is remapped to range [0, 255].</p>
<p>Module #2: Detect Nuclei</p> 	<p>1. Nucleus diameter (in pixels): Set this parameter to a roughly estimate diameter in pixels of all nuclei in your image.</p> <p>2. Image noise level: This parameter controls the trade-off between sensitivity and specificity. If you have a relative noisy image, use a hard level (=3), otherwise, use moderate (=2) or soft (=1) accordingly.</p> <p>3. Z to X-Y relative resolution: This is the resolution of the Z-axis divided by the resolution of the X-Y axis. Normally (for example with laser scanning confocal data) the Z resolution is lower, so this value should be between 0 and 1. You should know this information from the experimental settings used to acquire your image data.</p>

Module #3: Segment Nuclei



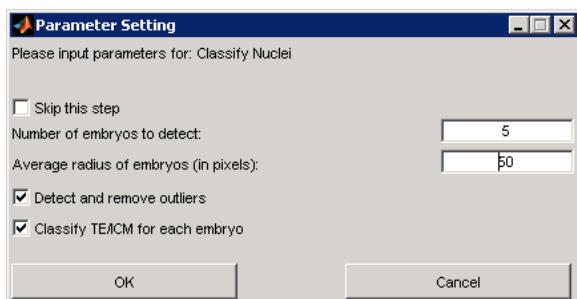
1. Image smoothing kernel:

This parameter controls the level of smoothness. Using 1.2 works well in practice for most mouse embryo and ES cell data.

2. Z to X-Y relative resolution:

This value lies between 0 and 1. In most cases, the Z-resolution will be lower than the X-Y resolution. If so, set this parameter to the value of $\{\text{resolution of X-Y panel}\}/\{\text{resolution of Z axis}\}$. For example, if your data is generated with 50 μm resolution in the X-Y, and 200 μm resolution along the Z axis, this parameter will be $50/200=0.25$.

Module #4: Classify Nuclei



1. Number of embryos to detect:

To separate multiple embryos, first specify the number of embryos existing in your image.

2. Average radius of embryos:

Also specify the average radius of embryos. Use a rough estimate.

3. Detect and remove outliers:

Check this will incur outer removal.

4. Classify TE/ICM for each embryo:

Check this will incur TE/ICM classification for each detected embryo.

SUPPLEMENTAL REFERENCES

- Appel, K., and Haken, W. (1989). Every planar map is four colorable, Vol 98 (Providence, RI, American Mathematical Society (AMS)).
- Artus, J., Panthier, J.J., and Hadjantonakis, A.K. (2010). A role for PDGF signaling in expansion of the extra-embryonic endoderm lineage of the mouse blastocyst. *Development* 137, 3361-3372.
- Bai, X., and Sapiro, G. (2007). A geodesic framework for fast interactive image and video segmentation and matting. Paper presented at: IEEE: International Conference on Computer Vision (ICCV) (Rio De Janeiro, Brazil).
- Brelaz, D. (1979). New methods to color the vertices of a graph. In *Communications of the ACM*, pp. 251-256.
- Couprie, C., Grady, L., Najman, L., and Talbot, H. (2010). Power Watersheds: A Unifying Graph-Based Optimization Framework. *IEEE Trans Pattern Anal Mach Intell*.
- Criminisi, A., Sharp, T., and Blake, A. (2008). Geos: Geodesic image segmentation. Paper presented at: European Conference on Computer Vision (Marseille, France).
- Fitzgibbon, A., Pilu, M., and Fisher, R.B. (1999). Direct least square fitting of ellipses. *IEEE Transactions on Pattern Analysis and Machine Intelligence (TPAMI)* 21, 476-480.
- Forsyth, D., and Ponce, J. (2002). *Computer Vision: A Modern Approach*.
- Gonzales, R.C., and Woods, R.E. (2008). *Digital Image Processing* (Upper Saddle River, NJ, Pearson Prentice Hall).
- Hassouna, M.S., and Farag, A.A. (2007). Multi-stencils fast marching methods: a highly accurate solution to the eikonal equation on cartesian domains. *IEEE Trans Pattern Anal Mach Intell* 29, 1563-1574.
- Kang, M., Xenopoulos, P., Muñoz-Descalzo, M., Lou, X., and Hadjantonakis, A.K. (2013). Live imaging, identifying and tracking single cells in complex populations in vivo and ex vivo. In *Methods in Molecular Biology*, K. Turksen, ed. (Germany, Springer-Verlag).

Lou, X., Koethe, U., Wittbrodt, J., and Hamprecht, F.A. (2012). Learning to Segment Dense Cell Nuclei with Shape Prior. Paper presented at: IEEE:Conference on Computer Vision and Pattern Recognition (CVPR) (Providence, RI).

Mereau, A., Grey, L., Piquet-Pellorce, C., and Heath, J.K. (1993). Characterization of a binding protein for leukemia inhibitory factor localized in extracellular matrix. *J Cell Biol* 122, 713-719.

Nichols, J., Silva, J., Roode, M., and Smith, A. (2009). Suppression of Erk signalling promotes ground state pluripotency in the mouse embryo. *Development* 136, 3215-3222.

Plusa, B., Piliszek, A., Frankenberg, S., Artus, J., and Hadjantonakis, A.K. (2008). Distinct sequential cell behaviours direct primitive endoderm formation in the mouse blastocyst. *Development* 135, 3081-3091.

Ringel, G., and Youngs, J.W. (1968). Solution of the heawood map-coloring problem. *Proc Natl Acad Sci U S A* 60, 438-445.

Sethian, J.A. (1996). A fast marching level set method for monotonically advancing fronts. *Proc Natl Acad Sci U S A* 93, 1591-1595.